International Journal of ISSI, Vol. 21(2024), No. 1, pp. 15-23

Online ISSN: 2981-0396 Print ISSN: 2981-0388

International Journal of Iron & Steel Society of Iran

Journal Homepage: https://journal.issiran.com/

Research Article

Microstructure and Corrosion Behavior of Friction Stir-Welded DP600 Steel

H. Ashrafi *[1], **M. Mohammadi** [2]

Faculty of Chemical and Materials Engineering, Shahrood University of Technology, Shahrood, Iran

ARTICLE INFO

Keywords:

Dual-Phase Steel, Friction Stir Welding, EBSD Characterization, Microstructure, EIS, Polarization.

Article history:

Received 16 September 2023
Received in revised form 20 September 2024
Accepted 20 November 2024

ABSTRACT

This study examined the microstructure and corrosion characteristics of friction stir welded DP600 steel. Two different combinations of rotational and transverse speeds were used for the welding process: 700 rpm and 80 mm/s (700-80 sample), and 1000 rpm and 20 mm/s (1000-20 sample). Microstructural observations demonstrated the formation of a mixture of polygonal ferrite, Widmanstatten ferrite (WF), bainite, and ferrite-carbide aggregate in the stir zone (SZ) of the welded samples. Furthermore, a coarser microstructure and a higher fraction of WF and bainite were observed in the 1000-20 sample. Electron backscatter diffraction analysis revealed areas with higher kernel average misorientation values around the martensite islands in the DP600 steel and within the bainite and WF in the welded samples. Formation of bainite and WF in the SZ of the welded samples resulted in the increase of the fraction of low-angle grain boundaries from ~5% in the DP600 steel to ~ 60% in the 1000-20 sample. The study further investigated the corrosion behavior using polarization, electrochemical impedance spectroscopy, and immersion tests. The results indicated that the corrosion performance of the 700-80 sample was similar to that of the original DP600 steel, whereas the 1000-20 sample exhibited a degradation in corrosion behavior with a corrosion rate approximately twice that for the other two samples, mainly due to its coarser microstructure.

1. Introduction

The automotive industry has seen a growing demand for the use of dual-phase (DP) steels in recent years [1, 2]. DP steels are the most commonly used type of advanced high-strength steels (AHSS), with a unique microstructure consisting of martensite islands within a ferrite matrix. This distinctive microstructure results in outstanding mechanical properties, including continuous yielding, a high initial strain hardening rate, excellent formability, and high strength [3, 4].

The automotive industry utilizes DP steels for various applications, which require joining techniques. Resistant spot welding is commonly used to join automobile components, while laser welding is employed to join blanks before the stamping process [5]. However, research has shown that laser-welded DP steels often experience softening in the heat-affected zone (HAZ) and hardening in the fusion zone [6, 7]. To address these issues, some researchers have explored the use of friction stir welding (FSW) as an alternative method for the joining of DP steel sheets.

FSW is a solid-state joining technique that was developed in 1991 [8]. In this process, a rotary tool with

---

* *Corresponding Author*
Email: hashrafi@shahroodut.ac.ir
Address: Faculty of Chemical and Materials Engineering, Shahrood University of Technology, Shahrood, Iran
1. Assistant Professor, 2. Assistant Professor

DOI: http://10.22034/IJISSI.2024.2011682.1272
Published by ISSI (Iron & Steel Society of Iran)

a pin and shoulder is inserted into the interface of the workpieces and moved along the joint. The combination of the tool's translation and rotation causes material to move from the front to the back of the pin, resulting in a solid-state welded joint. FSW offers several advantages over fusion welding techniques, including improved mechanical and metallurgical properties of the weld, elimination of issues like cracking and porosity, no need for shielding gas or filler material, lower residual stresses, and minimal fumes and hazardous waste [8, 9]. Over the years, researchers have explored various aspects of FSW concerning DP steel welds. For example, Miles et al. [10] examined the formability of FS-welded DP590 steel sheets, Ashrafi et al. [11] studied how welding parameters affect the microstructure and tensile properties of FS-welded DP600 steel, Mahmoudiniya and Kestens [12] investigated texture changes in the stir zone (SZ) and thermomechanically affected zone of a FS-welded DP steel, and Ashrafi et al. [13] studied the impact of the FSW heat input on the microstructure, micro-texture and mechanical properties of SZ in a DP600 steel.

The corrosion resistance of DP steels is one of the important factors for their use in the automotive industry. These steels are exposed to oxygen and humidity during service, making corrosion a significant concern, especially in areas with high salt content or acid rain [14]. However, research on the corrosion properties of DP steels has been less extensive compared to their mechanical properties. Studies have shown that DP steels experience micro-galvanic corrosion between the ferrite and martensite phases. However, it has been reported that the corrosion rate of ferrite-martensite DP steels in a 3.5% NaCl solution is lower than that of ferrite-pearlite microstructures due to a weaker galvanic couple between the ferrite and martensite phases [15].

The purpose of this study was to assess the microstructure and corrosion characteristics of the FS welds of DP600 steel. To achieve this, two different sets of parameters were used to perform FSW on the DP600 steel sheet. The resulting microstructure and corrosion properties of the SZs were then examined and compared to those of the base metal (BM).

2. Materials and methods

In this study, a 2 mm thick sheet of DP600 steel with the chemical composition listed in Table 1. was used as the BM. Samples with the dimensions of 150 mm×40 mm were cut from the initial steel and joined together using FSW in a butt configuration along the rolling direction, with the parameters presented in Table 2. A WC-based material, as depicted in Fig. 1. was used as the tool, with a tilt of 3° from the plate's normal and a plunge depth of 0.2 mm. Before the welding, the samples underwent mechanical cleaning, de-scaling, and degreasing with acetone.

The optical microscopy (OM) technique was used to examine the microstructure of welds. The cross-sections of the welds were observed using a Nikon EPHIPHOT300 microscope. To prepare the specimens for the microstructural analysis, they were first ground with SiC abrasive papers up to a grit size of 1200. Then, they were polished using a 0.3 μm alumina suspension and finally etched using a 2% Nital reagent. Electron backscatter diffraction (EBSD) examinations were conducted using a field emission scanning electron microscope (FESEM) equipped with a Nordlys Nano Oxford detector. Before the EBSD tests, the surfaces of the specimens were polished with a colloidal silica slurry with a particle size of 0.04 μm . EBSD patterns were obtained using AZTEC 2.0 data acquisition software, with a binning of 5×5 pixels. The raw data obtained was then processed using ATEX software [16].

Specimens with a dimension of 5 mm × 5 mm were cut from the BM and SZ of different welds for corrosion tests. Before electrochemical tests, specimens were ground up to 1200 grit finish followed by polishing with the 0.3 μm alumina suspension. The corrosion properties of samples were examined using an Ivium Vertex-One electrochemical instrument. To carry out both polarization and impedance measurement, a conventional three-electrode cell setup was used in this study. The setup consisted of a saturated calomel electrode (SCE) as the reference electrode, platinum as the counter electrode, and the coated sample as the working electrode. The electrochemical test was conducted in a solution containing 3.5 wt.% NaCl at room temperature. To stabilize the value of open-circuit potentials (OCP), all samples were submerged in the solution for 3 hours. Polarization measurement was then carried out with a scan rate of 1mV/s, and the values of E_{corr} and I_{corr} were obtained using the Tafel extrapolation method. For impedance spectroscopy investigation, an input voltage of 10mV was applied over a frequency range of 100 kHz to 10 mHz.

Table 1. The chemical composition of the DP600 steel sheet used in this research.

C	Mn	Si	S	P	Ni	Mo	Cu	V	Al	Co	Nb	Zr	Fe
0.18	1.25	0.2	0.01	0.011	0.015	0.019	0.019	0.02	0.073	0.045	0.023	0.011	Bal.

Table 2. Parameters of FSW operations.

Sample code	Rotational Speed (rpm)	Transverse Speed (mm/min)
700-80	700	80
1000-20	1000	20

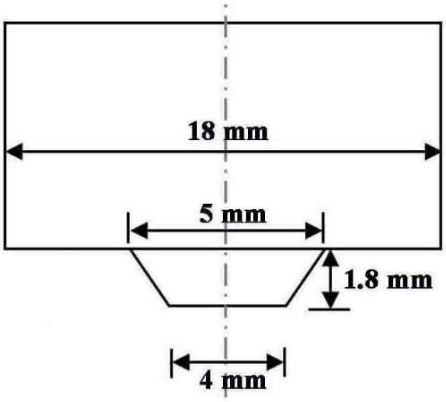

Fig. 1. Schematic diagram of the FSW tool.

3. Results and discussion

3.1. Microstructural observations

The microstructure and phase analysis results of the DP600 steel are shown in Fig. 2. The OM image in Fig. 2a. reveals that the microstructure of DP600 steel consists of unevenly distributed martensite islands (dark areas) within a ferrite matrix (bright areas). The X-ray diffraction (XRD) pattern of the DP600 steel in Fig. 2b. only indicates the presence of body-centered cubic (bcc) phase. Since low-carbon martensite has the same crystal structure as ferrite (i.e., bcc) [17], the XRD peaks should correspond to both ferrite and martensite. The XRD peaks of retained austenite were not detected due to its negligible amount. The phase map obtained from the EBSD measurements, shown in Fig. 2c. confirms the presence of ferrite and less than 0.1% retained austenite, consistent with the XRD results. It is important to note that ferrite and martensite cannot be distinguished on EBSD patterns due to their similar bcc structure. However, they can be differentiated based on their band contrast (BC) values. The martensite phase has a high crystal lattice distortion, resulting in a faint Kikuchi pattern [18, 19], and appearing dark in the BC map shown in Fig. 2d. Therefore, the dark areas in the BC map represent martensite islands predominantly located at grain boundaries of polygonal ferrite (PF). Additionally, it can be observed that these martensite islands are mainly positioned at triple junctions. Based on the EBSD phase analysis, the volume fraction of the martensite in the studied DP steel was approximately 22%.

Fig. 3. illustrates the microstructure of the SZ in the FS-welded samples. In the 700-80 sample (Fig. 3a.), the microstructure consists of a combination of PF, Widmanstatten ferrite (WF), bainite, and ferrite-carbide aggregate (FCA). The FCA is composed of small cementite particles dispersed in a ferrite matrix and forms under similar cooling rates as WF [20]. In the 1000-20 sample (Fig. 3b.), the micro-constituents were similar to those in the 700-80 sample, but the microstructure was coarser with a noticeable increase in WF and bainite and a decrease in PF and FCA fractions. The phase maps shown in Figs. 3c and 3d. only indicate the presence of bcc ferrite. No retained austenite was detected in the SZs. The brightness levels in the BC maps (Figs. 3e and 3f.) represent grains with different levels of BC. It is important to note that although PF, WF, and bainite are identified as bcc ferrite in the EBSD maps, their BC differs [21].

As measured in a previous study on the FWS of the current DP600 steel [11], the peak temperature in the SZ is higher than the critical temperature of A_3. Therefore, the microstructure is fully austenitic at the peak temperature. Due to a higher welding heat input in the 1000-20 sample, the peak temperature in the SZ is higher and therefore the austenite in this sample has a larger grain size. Large austenite grain size and relatively fast cooling rate lead to the formation of bainite, WF, and FCA besides PF. On the other hand, in the 700-80 sample, due to a lower peak temperature and therefore finer austenite grains, a larger fraction of PF forms during the cooling cycle. Furthermore, because of the higher cooling rate in the 700-80 sample, its microstructure is finer than that in the 1000-20 sample.

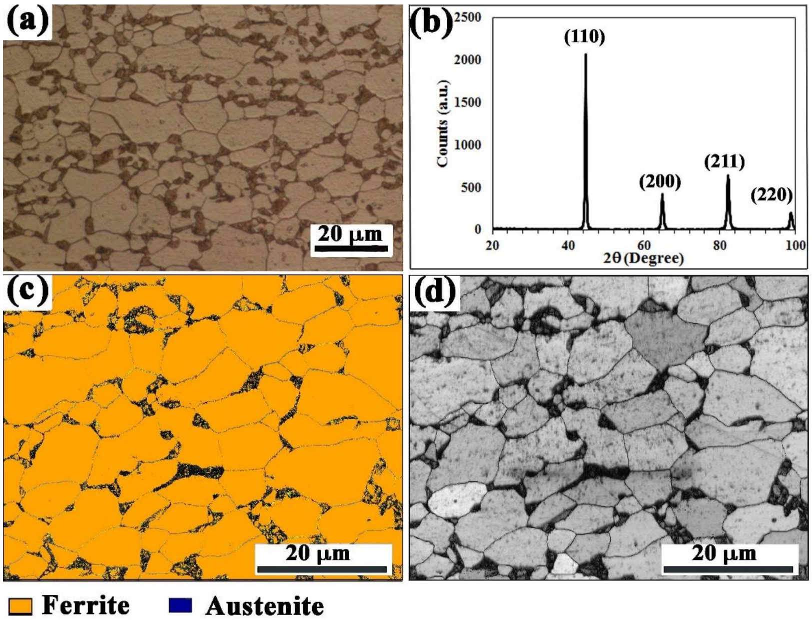

Fig. 2. Microstructure and phase analysis of the DP600 steel: (a) OM, (b) XRD pattern, (c) phase map, and (d) BC map.

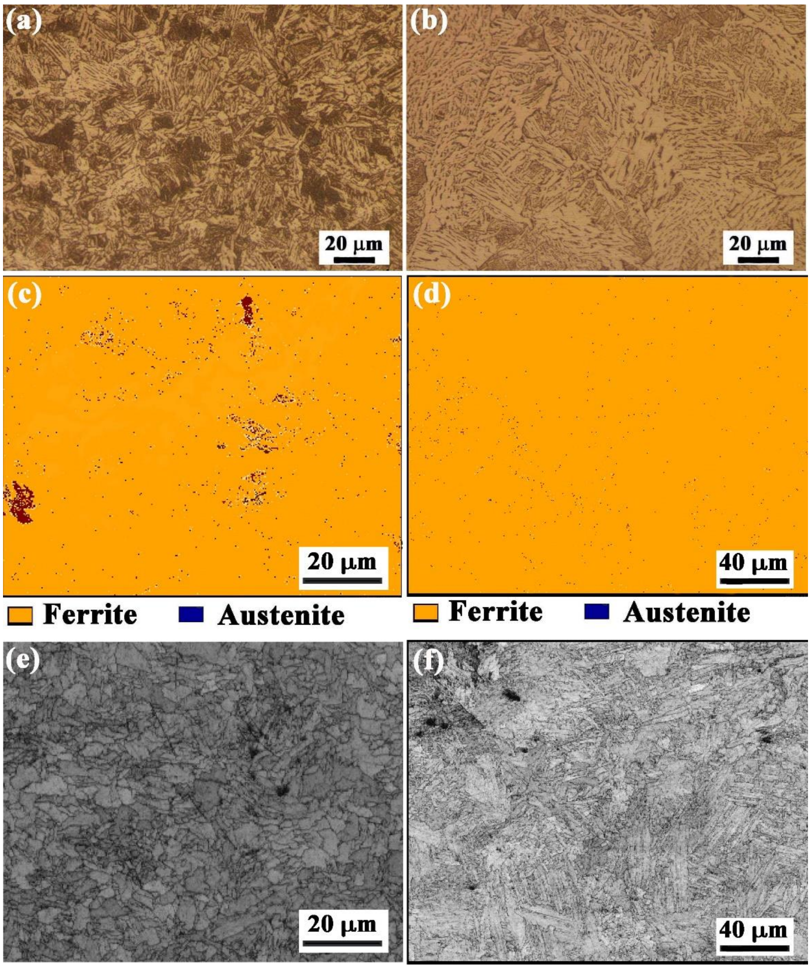

Fig. 3. OM image (a) and (b), phase map (c) and (d), and BC map (e) and (f) of the SZ for (a) & (c) & (e) 700-80 sample; (b) & (d) & (f) 1000-20 sample. Red pixels in the phase maps (c & d) are non-indexed points.

Fig. 4. displays the Kernel Average Misorientation (KAM) and Grain Boundary (GB) maps. KAM represents the average misorientation between a specific point and its neighboring points within a grain. It serves as an indicator of dislocation density and can be used to establish a connection between plastic deformation and misorientation within the microstructure. Grains that have undergone plastic deformation exhibit KAM values higher than 1° due to the presence of a high dislocation density, while recrystallized grains have KAM values smaller than 1° [22]. In the KAM map of the DP600 steel shown in Fig. 4a. the martensite phase is highlighted in red due to its significant lattice distortion. Additionally, most of the grains have KAM values below 0.5°, indicating a recrystallized structure. The ferrite matrix exhibits high KAM values (represented by white color) around the martensite islands rather than within the ferrite grains. This observation aligns with previous studies [23, 24], which attributed the formation of dislocation pile-up near the martensite phase to stresses resulting from austenite to martensite transformation. Due to the introduction of high stored energy by dislocations, the distorted ferrite matrix surrounding the martensite islands will likely dissolve preferentially.

The KAM map of the 700-80 and 1000-20 samples, shown respectively in Figs. 4c and d. indicate regions with high KAM values (represented by blue and white colors). This suggests that the transformation of austenite to bainite leads to the formation of geometrically necessary dislocations in the bainitic phase, increasing the KAM value [25]. Therefore, the areas with high KAM values in both samples are associated with the presence of bainitic regions. The GB map of the DP600 steel (Fig. 4b.) reveals that the majority of the grain boundaries (>95%) are high-angle GBs (HAGBs), while Figs. 4d and f. show that the fraction of the low-angle GBs (LAGBs) is higher in the SZs (~30% in the 700-80 and ~60% in the 1000-20 samples) compared to the BM. This increase in the fraction of LAGBs can be attributed to the higher volume fraction of the displacive transformation products such as bainite and WF. EBSD studies have demonstrated that the misorientation angle between ferrite laths in the bainite and WF is less than 10° [26, 27].

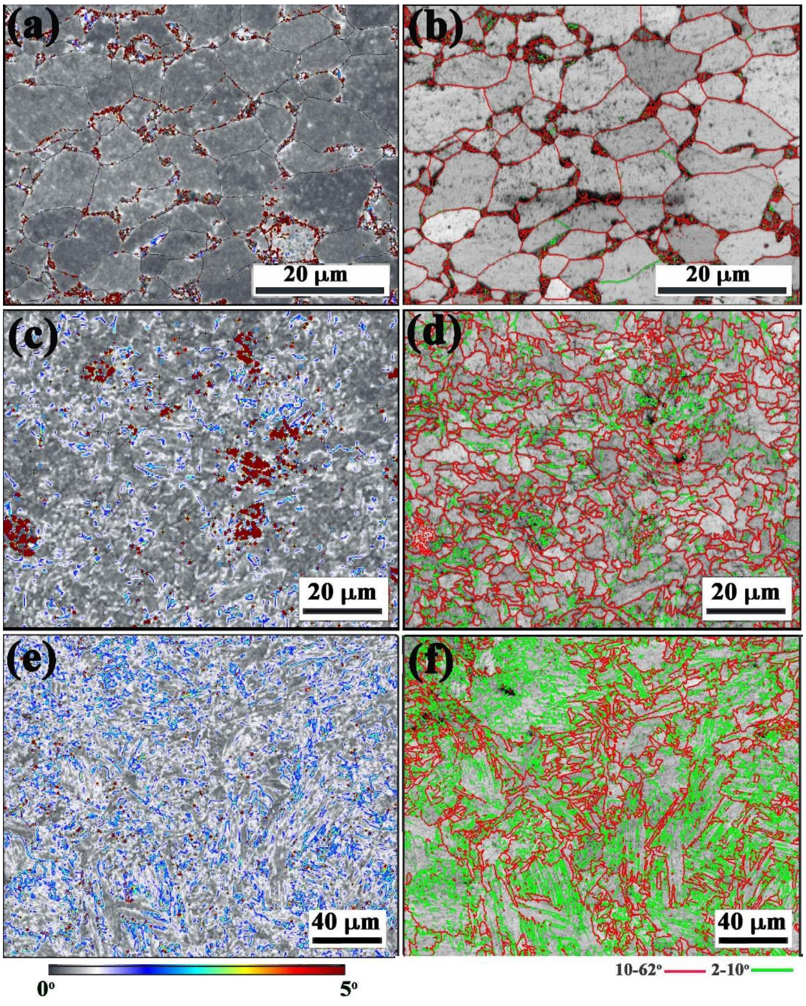

Fig. 4. KAM and GB map for (a) & (b) DP600 steel, (c) & (d) 700-80, (e) and (f) 1000-20.

3.2. Electrochemical corrosion behavior

The corrosion resistance of the DP600 steel and the welded joints was assessed through OCP, potentiodynamic polarization, and EIS measurements during an immersion test in the 3.5% NaCl solution. Fig. 5. demonstrates the variations in the OCP during the immersion test as a function of time. At the outset, the OCP decrement rate is high for all samples, but as the exposure time progresses, this rate gradually decreases until it becomes almost constant, after 80 min immersion. These variations in the OCP can be attributed to the change in the surface properties such as the formation or dissolution of corrosion products on the specimen surface during immersion in the corrosive salt [28, 29]. The sample labeled 1000-20 has the lowest OCP value, while the 700-80 sample has the highest, indicating that the 700-80 sample has better stability compared to both the DP600 steel and the 1000-20 samples. Thermodynamic stability of the samples in the corrosive media can be obtained by the study of OCP variations. In other words, the OCP varies with time because of the change in the oxidation tendency of the sample surface.

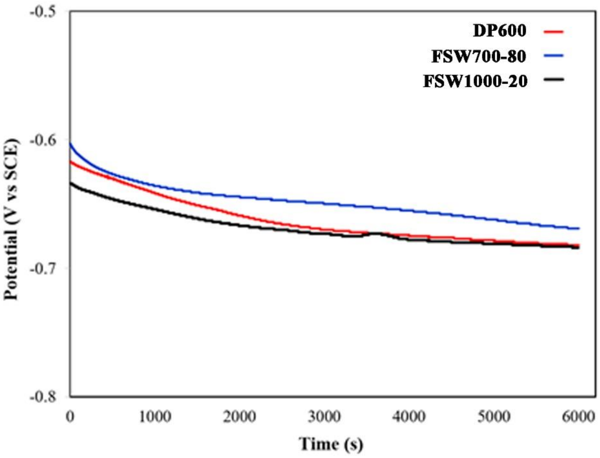

Fig. 5. OCP variation of the BM and FS welded sample.

Fig. 6. shows the typical potentiodynamic polarization curves obtained for samples after 3 hours of immersion in the 3.5wt.% NaCl aqueous solution. Passivation behavior is not observed in any of the samples; Indeed, the absence of passivation behavior can be expected based on the chemical composition of the DP600 steel. The electrochemical parameters such as cathodic and anodic slope, corrosion current density (I_{corr}), and corrosion potential (E_{corr}) of the tested samples obtained by the Tafel analysis method are presented in Table 3. It is evident that the corrosion potential of DP600 and FSW700-80 samples are close to each other, and the welding process has not had a significant impact on the corrosion potential of this sample. The changes in corrosion potential are more evident in the FSW1000-20 sample. A higher negative potential indicates a greater tendency to participate in electrochemical reactions. The lower corrosion rate is obtained for the FSW700-80 sample (8.3 μA/cm^2), which is close to that for the DP600 steel. The corrosion rate of the FSW1000-20 sample is increased by about two times compared to DP600 and FSW700-80 samples. As previously mentioned, the microstructure of the DP600 steel mainly consists of martensite islands distributed along the boundaries of the ferrite grains. Additionally, a significant number of dislocations was observed around the martensite islands. According to Chen et al. [30], When dual-phase (DP) steels are exposed to a corrosive solution, the chemical potential difference between the martensite and ferrite phases leads to the formation of micro-galvanic cells. This phenomenon results in the localized anodic dissolution of the ferrite matrix.

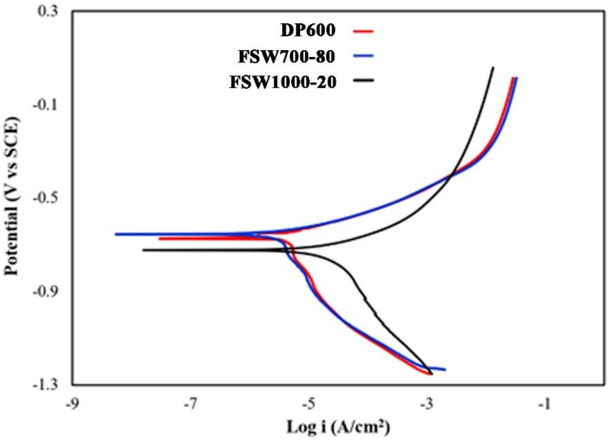

Fig. 6. Potentiodynamic polarization curves of the DP600 steel and SZs in 3.5% NaCl aqueous solution.

In the 700-80 and 1000-20 samples, different micro-constituents like PF, bainite, WF, and FCA are present. In electrochemical studies, the presence of multiphase structures facilitates the occurrence of galvanic corrosion. The difference in the electrochemical potential between the cementite particles within the FCA

Table 3. Corrosion parameters obtained in the test with a 3.5% NaCl solution.

Specimen	E_{corr} (V vs SCE)	I cor. (μA/cm^2)	Rp (Ω.cm^2)	Corr. Rate (mm/y)
DP600	-0.66	9.2	1.98×10^4	0.0038
FSW700-80	-0.65	8.3	2.37×10^4	0.0035
FSW1000-20	-0.72	17.4	0.786×10^4	0.0074

compared to the ferrite in the 1000-20 sample can lead to the formation of the galvanic microcells that enhance the ferrite corrosion, resulting in the higher corrosion current density. A similar effect can be observed in the cementite particles within the ferrite laths in the bainite, thus accelerating the corrosion rate. The lower corrosion rate in the 700-80 sample can be attributed to its smaller grain size and more homogeneous microstructure, which increases the resistance to penetration of corrosive ions [31]. Additionally, a finer grain size leads to a more uniform distribution of phases in the steel matrix, bringing the anode and cathode areas closer together [32].

Fig. 7. shows the electrochemical impedance spectroscopy (EIS)-Nyquist plots of the BM and SZ specimens in the 3.5 % NaCl solution. All plots show a single depressed semicircle shape, indicating that the electrode reaction is controlled only by a charge transfer process. The larger ring shows a higher impedance value and higher corrosion resistance. The capacitance arc diameter (Rct), a measure of corrosion resistance, can be ranked in increasing order as FSW1000-20 < DP600 < FSW700-80, which aligns well with the polarization results.

Fig. 8. exhibits OM images depicting the corroded surfaces of the specimens following a 3-hour immersion and polarization test in the 3.5% NaCl solution. A comparison between the specimens reveals that the surface of the 1000-20 specimen experiences more extensive corrosion, which aligns with the electrochemical findings. In the case of the DP600 steel (Fig. 8a.), there are crevices present along the ferrite-ferrite and ferrite-martensite boundaries. This indicates a preferential dissolution of the ferrite matrix adjacent to these boundaries. Importantly, Chen et al. [30] have highlighted that such preferential dissolution of the surrounding ferrite can result in the detachment of martensite islands. Furthermore, the 700-80 specimen demonstrates a greater severity of corrosion attack in the ferrite regions of FCA and bainite compared to the PF. As previously stated, the corrosion mainly occurs through the creation of small galvanic cells between the ferrite and cementite phases. It appears that when the cementite particles are evenly distributed within the ferrite matrix, the dissolution of the anode (ferrite) decreases. In comparison to the BM, the 700-80 specimen exhibited shallow and evenly distributed corrosion on the ferrite regions. In the 1000-20 specimen (Fig. 8c.), a severe corrosion attack was observed across the entire microstructure.

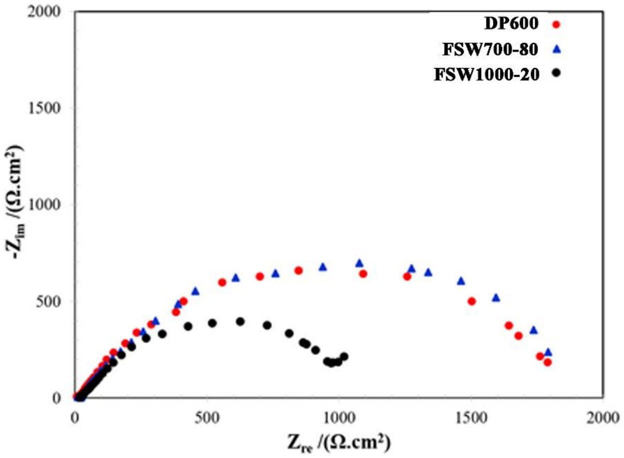

Fig. 7. EIS Nyquist plots of DP600 steel and FS welded samples in 3.5%NaCl solution.

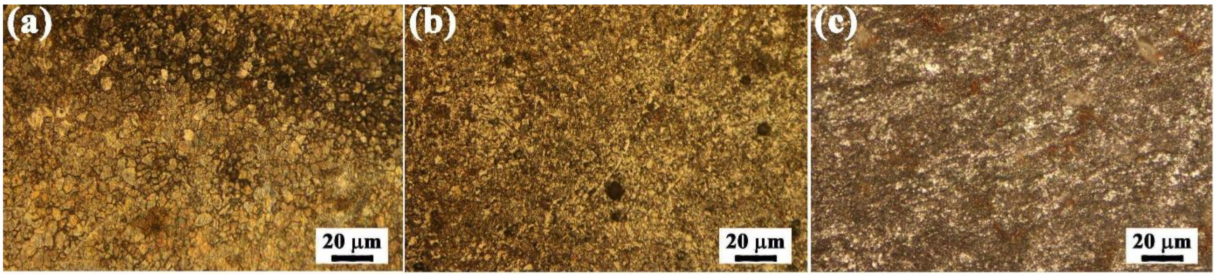

Fig. 8. Optical micrograph of the corrosion morphology for different samples after immersion and polarization test in the 3.5% NaCl solution for 3h, (a) DP600 steel, (b) 700-80, (c) 1000-20.

4. Conclusions

This study compared the microstructure and corrosion characteristics of the SZ in FS-welded DP600 steel with the respective BM. Microstructural analysis using OM and EBSD showed that the microstructure of the SZ in the FS-welded samples consisted of a combination of PF, WF, bainite, and FCA. The microstructure of the SZ in the 1000-20 sample was coarser than that in the 700-80 sample and the former had a larger fraction of displacive transformation products like bainite and WF than the latter, as a result of a larger prior austenite grain size. Regions with high KAM values, caused by the volume change during the transformation of austenite, were observed in the vicinity of the martensite islands in the microstructure of the DP600 steel, and within the bainite and WF laths in the microstructure of 700-80 and 1000-20 samples. Formation of bainite and WF resulted in a higher fraction of LAGBs in the SZs (~30% in the 700-80 sample and ~60% in the 1000-20 sample) compared to the DP600 steel BM (< 5%). The results obtained from polarization, EIS, and immersion tests indicated that the corrosion performance of the 700-80 sample was similar to that of the DP600 steel, while the 1000-20 sample exhibited worse corrosion performance than the other two samples. This degradation in corrosion performance can mainly be attributed to the coarse microstructure in this sample.

References

[1] Deng Y.G, Li Y, Di H, Misra R.D.K, Effect of heating rate during continuous annealing on microstructure and mechanical properties of high-strength dual-phase steel. J Mater Eng Perform. 2019; 28: 4556–64.

[2] Tian C, Kusche C.F, Medina A, Lee S, Wollenweber M.A, Pippan R, et al. Understanding the damage initiation and growth mechanisms of two DP800 dual phase grades. Mater Des. 2024; 238: 112630.

[3] Ashrafi H, Shamanian M, Emadi R, Saeidi N, Correlation of tensile properties and strain hardening behavior with martensite volume fraction in dual-phase steels. Trans Indian Inst Met. 2017; 70: 1575–84.

[4] Deng Y.G, Yang Y.P, Fine-grained dual-phase steels fabricated via cold-rolling ferrite-martensite structure and subsequent intercritical annealing, J Mater Res Technol. 2023; 27: 3881-6.

[5] Ashrafi H, Shamanian M, Emadi R, Sarmadi M.A, Comparison of microstructure and tensile properties of dual phase steel welded using friction stir welding and gas tungsten arc welding. Steel Res Int. 2018; 89: 1700427.

[6] Jia Q, Guo W, Li W, Peng P, Zhu Y, Zou G, et al. Experimental and numerical study on local mechanical properties and failure analysis of laser welded DP980 steels, Mater Sci Eng A. 2017; 680: 378–87.

[7] Bandyopadhyay K, Panda S.K, Saha P, Investigations into the influence of weld zone on formability of fiber laser-welded advanced high strength steel, J Mater Eng Perform. 2014; 23: 1465–79.

[8] Gibson B.T, Lammlein D.H, Prater T.J, Longhurst W.R, Cox C.D, Ballun M.C, et al. Friction stir welding: process, automation, and control. J Manuf Process. 2014; 16: 56-73.

[9] Wu Q, Li M, Guo Y, Shan J, Wang H, Chang Y, Microstructural evolution and mechanical properties of friction stir welded 12Cr-ODS steel, Nucl Mater Energy. 2020; 25: 100804.

[10] Miles M.P, Pew J, Nelson T.W, Li M, Comparison of formability of friction stir welded and laser welded dual phase 590 steel sheets, Sci Technol Weld Join. 2006; 11: 384-8.

[11] Ashrafi H, Shamanian M, Emadi R, Sarmadi M.A, Effect of welding parameters on the microstructure and tensile properties of friction stir-welded DP600 steel, SAE Int J Mater Manuf. 2019; 12: 165-78.

[12] Mahmoudiniya M, Kestens L.A.I, Microstructural development and texture evolution in the stir zone and thermomechanically affected zone of a ferrite-martensite steel friction stir weld, Mater Charact. 2021; 175: 111053.

[13] Ashrafi H, Shamanian M, Sanayei M, Farhadi F, Szpunar J.A, the impact of welding heat input on microstructure, micro-texture, and mechanical properties of stir zone in friction stir welded DP600 steel, Mater Today Commun. 2023; 37: 107127.

[14] Vences-Herna´ndez R, Reyes-Caldero´n F, Villalobos J.C, Vergara-Herna´ndez H.J, Salazar-Torres J.A, Evaluation of corrosion susceptibility of conventional dual-phase steels used in the automotive industry, J Mater Eng Perform. 2020; 29: 6520–34

[15] Abedini O, Behroozi M, Marashi P, Ranjbarnodeh E, Pouranvari M, Intercritical heat treatment temperature dependence of mechanical properties and corrosion resistance of dual phase steel, Mater Res. 2019; 22: 20170969.

[16] Beausir B, Fundenberger J.J, Analysis Tools for Electron and X-ray diffraction, ATEX-software, www.atex-software.eu, Universite´ de Lorraine - Metz. (2017).

[17] Wang Y, Tomota Y, Ohmura T, Morooka S, Gong W, Harjo S, Real time observation of martensite transformation for a 0.4C low alloyed steel by neutron diffraction. Acta Mater. 2020; 184: 30-40.

[18] Li S, Guo C, Hao L, Kang Y, An Y, In-situ EBSD study of deformation behaviour of 600 MPa grade dual phase steel during uniaxial tensile tests. Mater Sci Eng A. 2019; 759: 624-32.

[19] Li Y, Song R, Jiang L, Zhao Z, Deformation response of 1200 MPa grade martensite-ferrite dual-phase steel under high strain rates, Mater Sci Eng A. 2019; 750: 40-4.

[20] Ashrafi H, Shamanian M, Emadi R, Saeidi N,

Microstructure, tensile properties and work hardening behavior of GTA-welded dual-phase steels, J Mater Eng Perform. 2017; 26: 1414-23.

[21] Wu J, Wray P.J, Garcia C.I, Hua M, Deardo A.J, Image quality analysis: a new method of characterizing microstructures, ISIJ Int. 2005; 45: 254-62.

[22] Lin H.P, Chen D, Kuo J.C, Grain boundary evolution of cold rolled FePd alloy during recrystallization at disordering temperature, Materials. 2015; 8: 3254–67.

[23] Ghassemi-Armaki H, Maaß R, Bhat S.P, Sriram S, Greer J.R, Kumar K.S, Deformation response of ferrite and martensite in a dual-phase steel, Acta Mater. 2014; 62: 197-211.

[24] Calcagnotto M, Ponge D, Demir E, Raabe D, Orientation gradients and geometrically necessary dislocations in ultrafine grained dual-phase steels studied by 2D and 3D EBSD, Mater Sci Eng A. 2010; 527: 2738–46.

[25] Zaefferer S, Romano P, Friedel F, EBSD as a tool to identify and quantify bainite and ferrite in low-alloyed Al-TRIP steels, J Microsc. 2008; 230: 499–508.

[26] Phelan D, Dippenaar R, Widmanstätten ferrite plate formation in low-carbon steels, Metal Mater Trans A. 2004; 35: 3701-6.

[27] Wei L, Nelson T.W, Influence of heat input on post weld microstructure and mechanical properties of friction stir welded HSLA-65 steel, Mater Sci Eng A. 2012; 556: 51-9.

[28] Wang Z.F, Li P.H, Guan Y, Chen Q.F, Pu S.K, The corrosion resistance of ultra-low carbon bainitic steel, Corr Sci. 2009; 51: 954-61.

[29] Guo J, Yang S, Shang C, Wang Y, He X, Influence of carbon content and microstructure on corrosion behaviour of low alloy steels in a Cl containing environment, Corr Sci. 2008; 51: 242-51.

[30] Chen H, Lv Z, Lu L, Huang Y, Li X, Correlation of micro-galvanic corrosion behavior with corrosion rate in the initial corrosion process of dual phase steel, J Mater Res Technol. 2021; 15: 3310-20.

[31] Ghanem W.A, Hussein W.A, AbouShahba R.A, Morad M.M, The corrosion behavior of ferrite bainite dual phase steel in 3.5% NaCl solution, Middle East J Appl Sci. 2016; 6: 627-35.

[32] Guo Y.b, Li C, Liu Y.c, Yu L.m, Ma Z.q, Liu C.x, et al. Effect of microstructure variation on the corrosion behavior of high-strength low-alloy steel in 3.5wt% NaCl solution, Int J Miner Metall Mater. 2015; 22: 604-12.